A Dynamic Model of a High-Temperature Arc Lamp

Basia Halliop, Francis P. Dawson, *Fellow, IEEE*, and Mary C. Pugh

Abstract—**High-temperature high-pressure arc lamps are used to thermally process semiconductor wafers. An accurate dynamic model that links the radiation output to the current input would facilitate the design of a power circuit that optimizes energy transfer to the arc. In this paper, a dynamic arc model is derived using averaging of the energy balance equation over spatial domains. This space averaging approach (the "finite-volume method") accurately models the energy balance equation, as tested with both steady and transient arc currents, including high-energy pulses with a current amplitude range from 400 A to 27 kA and a pulsewidth of a millisecond or less.**

Index Terms—**Arc lamp, finite-volume method (FVM).**

I. INTRODUCTION

A HIGH-TEMPERATURE high-pressure arc lamp is used for rapid thermal processing of semiconductor wafers. The lamp uses rapid pulses of optical radiation to heat the surface of the wafer to a high temperature in a short period of time, thus limiting diffusion of materials into the wafer. The current through the arc is pulsed from a simmer current of approximately 400 A to as much as 27 kA and back in a time on the order of 1 ms [1]. Power circuits that can control the flow of energy to the arc are required to power the lamp in order to obtain the desired wafer temperature distribution. An accurate dynamic model of the argon arc that links the radiation output to the current input would aid in the design of such power circuits.

Existing arc models that are used in power circuit designs are empirical. The coupling between the electric and heat flux density fields is not included. Therefore, the temporal evolution of the optical output cannot be determined.

Existing design procedures for designing pulse-forming networks for Flash lamps are based on a quasi-steady-state model of the arc. For example, for a single-mesh L/C drive circuit, Markiewicz and Emmett have defined formulas [see (1)–(5)] to describe the lamp's electrical behavior and to choose appropriate L and C values [2] (see also [3, p. 14]). The arc voltage is assumed to be given by

$$v = \pm K_o(i)^{0.5}. \tag{1}$$

B. Halliop and F. P. Dawson are with the Department of Electrical and Computer Engineering, University of Toronto, Toronto, ON M5S 3G4, Canada (e-mail: basia.halliop@utoronto.ca; dawson@ele.utoronto.ca).

M. C. Pugh is with the Department of Mathematics, University of Toronto, Toronto, ON M5S 2E4, Canada (e-mail: mpugh@math.utoronto.ca).

This equation is used to describe the arc if the current density i is greater than 500 A/cm^2. The impedance parameter is K_o and is modeled by

$$K_o = 1.28 \left(\frac{P}{K_1} \right)^{0.2} \frac{l_{\text{arc}}}{d} \tag{2}$$

where P is the fill pressure (in torr), l_{arc} is the arc length (in millimeters), d is the bore diameter (in millimeters), and K_1 is a constant, which depends on the gas in question.

Given the arc characterization in (1) and (2), the capacitor value for a simple L/C pulser can then be chosen as

$$C_{\text{ch}} = \frac{[2U_{\text{ch}} a^4 \tau^2]^{0.33}}{K_o^4} \tag{3}$$

where U_{ch} is the stored energy (in joules); a is a damping parameter, which is 0.8 for critical damping; and τ is a time parameter (in seconds), corresponding to 1/3 of the desired pulsewidth. If the pulse is approximately sinusoidal, then the pulsewidth can be described as half a period of a sinusoidal wave. Thus, τ is 1/6 of the period or approximately $1/2\pi$ times the period, leading to

$$L_{\text{ch}} = \frac{\tau^2}{C_{\text{ch}}}. \tag{4}$$

The initial voltage V_{ch} across the storage capacitor can be calculated as

$$V_{\text{ch}} = \left(\frac{2U_{\text{ch}}}{C} \right)^{0.5}. \tag{5}$$

Equations (1)–(5) give good first-order approximations and can be used to predict the shapes of current pulses [3], although they do not incorporate arc dynamics. This type of modeling approach cannot be used to optimize the pulse-forming network for optimum energy transfer from the electrical supply to the wafer via infrared radiation.

A number of mathematical models exist to describe dynamic arc behavior. The most commonly used arc models are the Cassie, Mayr, and Cassie–Mayr models. Other existing dynamic models are primarily modifications or combinations of these models [4].

A. Cassie Model

Cassie investigated high-current arcs and assumed that their power losses are mainly a result of convection losses [5]. The arc is assumed to maintain a relatively constant temperature and conductivity, and as the current i increases, the arc diameter

increases, leading to an increase in conductance G_c. The Cassie model is represented by

$$\frac{1}{G_c}\frac{d}{dt}G_c = \frac{1}{\theta}\left(\frac{iv}{G_c E_{ss}^2} - 1\right). \qquad (6)$$

In the preceding equation, E_{ss} is the steady-state electric field, and v is the arc voltage. The arc time constant θ is given by the ratio of energy stored U_{arc} to power loss Q_{loss}, i.e.,

$$\theta = \frac{U_{arc}}{Q_{loss}}. \qquad (7)$$

B. Mayr Model

Mayr investigated small-current arcs and assumed that thermal conduction is the primary form of power loss [6]. In this case, the cross-sectional area of the arc does not have a strong impact on the arc conductance and can be assumed to be constant. In Mayr's arc model,

$$\frac{1}{G_m}\frac{d}{dt}G_m = \frac{1}{\theta}\left(\frac{iv}{Q_{loss}} - 1\right) \qquad (8)$$

electrical conductivity is dependent on temperature, and temperature varies in both time and space. Mayr modeled power loss Q_{loss} as constant.

C. Cassie–Mayr Model

The Cassie model is valid primarily at high currents and the Mayr model at very small currents. To cover a larger range of arc behavior, the Cassie and Mayr models may be combined. This may be accomplished in different ways. In the case where G_c and G_m can be isolated or approximated, they can be combined in series [4] as

$$\frac{1}{G_{cm1}} = \frac{1}{G_c} + \frac{1}{G_m}. \qquad (9)$$

The conductance G_{cm1} will be dominated by the Cassie conductance G_c in the high-current regime and by the Mayr conductance G_m in the small-current regime, with a smooth transition in between.

Another model [7] that combines Cassie and Mayr behavior is

$$\frac{1}{G_{cm2}}\frac{d}{dt}G_{cm2} = \frac{1}{\theta_0(G_{cm2})^\beta}\left(\frac{iv}{N_0(G_{cm2})^\alpha} - 1\right). \qquad (10)$$

Here, the time constant θ and the power loss Q_{loss} are both assumed to vary with the conductance, i.e., $\theta = \theta_0(G_{cm2})^\beta$, and the power loss is $Q_{loss} = N_0(G_{cm2})^\alpha$. The constants θ_0, β, N_0, and α are experimentally determined.

Models derived from physical principles can give more accuracy for a greater range of situations and can be used to better predict wafer heating. A model that can be represented in a circuit or state-space form and imported as a macro into a circuit simulator would also be valuable. This paper presents a dynamic partial differential equation (PDE) model of a high-pressure arc lamp that is derived from first principles. A finite-
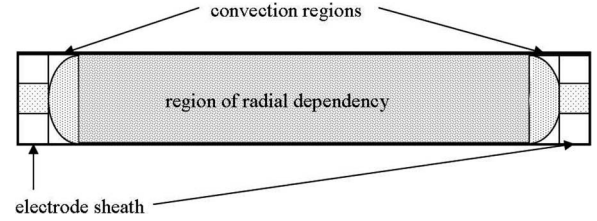

Fig. 1. View of lamp showing end effects and conduction regions. In the region marked "radial dependency," the temperature is approximated as being independent of length and angle.

dimensional arc model is then derived using averaging of the energy balance equation over spatial domains. This model can be designed to meet a specific accuracy requirement.

One contribution of this paper is to present the method for deriving a space-averaged arc model. The method used is one that employs physical and geometric data to set the coefficients in modeling, thus avoiding the problem of system identification. The resulting model is in a form that can be expressed with a circuit while giving the expected voltage versus current and optical temporal output characteristics.

II. PDE MODEL

The lamp is cylindrical in shape with current flow in the axial direction, as shown in Fig. 1. It consists of a hollow quartz cylinder where argon gas is pumped in near the cathode and out near the anode. In this particular lamp, water is used for cooling and to protect the quartz tube; a stream of water is swirled around the inside surface of the quartz tube, creating a sheet of water between the argon arc and the quartz tube. In this paper, water is assumed to hold the outer edge of the arc at a constant temperature. In reality, the water wall will be partially vaporized, and thus, the lamp will be a mixture of argon and water vapor. However, such water-wall mixing is not considered here. End effects are initially neglected, as is the movement of gas along pressure gradients. The end effects can be treated separately, and then, the voltage drop across these regions can be added to the arc voltage. These assumptions imply that there is no heat or radiation flowing into or out of the arc in an axial direction, and hence, the arc has temperature dependence only in the radial direction. A main goal of this paper is to demonstrate the modeling concept: the modeling process can be generalized to the full 3-D model, as well as one that includes other coupling terms.

The law of conservation of energy is used as a basis for the model. The energy balance equation at any point in the lamp is

$$C_p(T)\rho(T)\frac{\partial T}{\partial t} - \nabla \cdot (\kappa(T)\nabla T) = \sigma(T)E^2 - 4\pi\epsilon_0(T) \qquad (11)$$

where T is the temperature, C_p is the specific heat capacity, ρ is the density, κ is the thermal conductivity, σ is the electrical conductivity, and ϵ_0 is the net radiative emissivity. The transport and thermodynamic coefficients are all nonlinear functions of temperature. The constitutive equation for the electric field is

$$E(t) = \frac{i_{in}(t)}{\iiint \sigma(T)dx\,dy\,dz} = \frac{i_{in}(t)}{G(t)} \qquad (12)$$
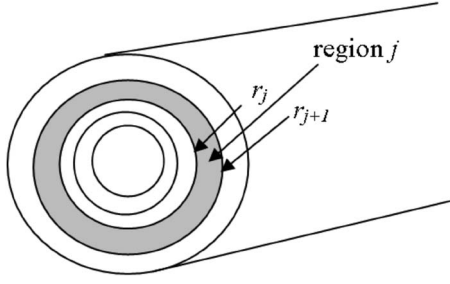
Fig. 2.   Problem domain and regions. The shaded region between $r = r_j$ and $r = r_{j+1}$ is region j. The average temperature in this region is denoted $T_{\mathrm{mid}j}$.

where the integral is over the volume of the arc. In the preceding equation, $i_{\mathrm{in}}(t)$ is the input current. The temperature is assumed constant on the arc walls, and an adiabatic boundary condition is applied on both ends of the arc.

III. FVM MODEL

Spatial integration of (11) and (12) is used to transform the PDE into a system of ordinary differential equations (ODEs). The lamp cross section is divided into a central cylinder, which is surrounded by nested concentric shells (see Fig. 2). An integrated energy equation is found for each of these regions. The temperature T is assumed independent of length and angle, resulting in equations defined per unit length.

Consider a shell with inner radius $\tilde{r}$ and outer radius $\tilde{r} + \Delta$. Integrating (11) over this shell and applying the divergence theorem yields

$$\overline{AC_p\rho\frac{\partial T}{\partial t}} - 2\pi r\kappa \left.\frac{\partial T}{\partial r}\right|_{\tilde{r}+\Delta} + 2\pi r\kappa \left.\frac{\partial T}{\partial r}\right|_{\tilde{r}} = A\left(\overline{\sigma E(t)^2} - 4\pi\overline{\epsilon_0}\right).$$
(13)

Here, $A = \pi((\tilde{r}+\Delta)^2 - \tilde{r}^2)$ is the cross-sectional area, and the overline denotes the cross-sectional average.

The first term on the left-hand side of (13) is the average of a product of functions. One wishes to approximate this with the product of the averages. If functions f and g are smooth enough, then $\overline{fg} = \bar{f}\bar{g} + \mathcal{O}(\Delta^2)$. Therefore, for a thin shell and a thin cylinder, the approximation

$$\overline{C_p\rho\frac{\partial T}{\partial t}} = \overline{C_p\rho}\,\overline{\frac{\partial T}{\partial t}} = \overline{C_p\rho}\,\frac{\partial \overline{T}}{\partial t}$$
(14)

is made, resulting in an ODE for the average temperature in a shell, i.e.,

$$A\overline{C_p\rho}\frac{\partial \overline{T}}{\partial t} = 2\pi r\kappa \left.\frac{\partial T}{\partial r}\right|_{\tilde{r}+\Delta} - 2\pi r\kappa \left.\frac{\partial T}{\partial r}\right|_{\tilde{r}} + A\left(\overline{\sigma E(t)^2} - 4\pi\overline{\epsilon_0}\right).$$
(15)

Similarly, integrating (11) over a cylinder of radius Δ and making the approximation (14) yields

$$A\overline{C_p\rho}\frac{\partial \overline{T}}{\partial t} = 2\pi r\kappa \left.\frac{\partial T}{\partial r}\right|_{\Delta} + A\left(\overline{\sigma E(t)^2} - 4\pi\overline{\epsilon_0}\right)$$
(16)

where $A = \pi\Delta^2$.

The lamp is divided into n regions, determined by the radii $0 = r_1 < r_2 < \ldots < r_n < r_{n+1} = R$, where R is the radius of the lamp. Introducing the notation

$$T_{\mathrm{mid}j}(t) = \frac{1}{A_j}\int_{r_j}^{r_{j+1}} T(r,t)dr$$
(17)

$$A_j = \pi\left(r_{j+1}^2 - r_j^2\right)$$
(18)

(15) and (16) result in n ODEs for $T_{\mathrm{mid}j}(t)$. The electric field $E(t)$ involves an integral over the entire lamp (12), and thus, the n ODEs are coupled to one another.

The right-hand sides of the ODEs (15) and (16) have conductive heat loss terms such as

$$2\pi r\kappa(T) \left.\frac{\partial T}{\partial r}\right|_{r_j}$$
(19)

for $2 \le j \le n + 1$. To have a closed system of ODEs, one needs to approximate these terms. A natural approximation of (19) would be

$$2\pi r_j \frac{\kappa\left(T_{\mathrm{mid}(j-1)}\right) + \kappa(T_{\mathrm{mid}j})}{2} \frac{T_{\mathrm{mid}j} - T_{\mathrm{mid}(j-1)}}{r_{\mathrm{mid}j} - r_{\mathrm{mid}(j-1)}}$$
(20)

where

$$r_{\mathrm{mid}j} = \frac{r_j + r_{j+1}}{2}.$$
(21)

If $r_j - r_{j-1} = r_{j+1} - r_j = \Delta$, then (20) is a good approximation of (19): their difference is $\mathcal{O}(\Delta^2)$. However, the expression (20) is not easily implemented in a circuit. For this reason, an approach based on thermal resistance is used to approximate (19). Consider a tube of length L with inner radius r_a and outer radius r_b. A steady state of the heat equation would satisfy

$$\nabla \cdot (\kappa(T)\nabla T) = 0.$$
(22)

Integrating this over the cylinder and assuming that the temperature T depends only on the radius r results in the flux

$$2\pi rL\kappa(T)\frac{dT}{dr} = Q$$
(23)

where Q is a constant. If the conductance is a linear function of temperature, $\kappa(T) = \kappa_0 + \kappa_1 T$, then the ODE (23) can be solved by separation of variables, resulting in

$$\kappa\left([T(r_b) + T(r_a)]/2\right)(T(r_b) - T(r_a)) = \frac{Q}{2\pi L}\ln(r_b/r_a).$$
(24)

Thermal resistance is defined via $T(r_b) - T(r_a) = QR_{\mathrm{therm}}$, thus yielding the thermal resistance per unit length

$$R_{\mathrm{therm}} = \frac{\ln(r_b/r_a)}{2\pi\kappa\left([T(r_b) + T(r_a)]/2\right)}.$$
(25)

This approach would result in the approximate conductive heat loss of

$$Q = \frac{T_{\mathrm{mid}j} - T_{\mathrm{mid}(j-1)}}{R_j}$$
(26)

with R_j given by

$$R_j = \frac{\ln\left(r_{\mathrm{mid}j}/r_{\mathrm{mid}(j-1)}\right)}{2\pi\kappa\left(\left[T_{\mathrm{mid}j} + T_{\mathrm{mid}(j-1)}\right]/2\right)}. \tag{27}$$

If $r_j - r_{j-1} = r_{j+1} - r_j = \Delta$, then (26) and (27) are a good approximation of (19): their difference is $\mathcal{O}(\Delta^2)$.

The ODE (15) has source terms on the right-hand side, arising from the source terms in the energy equation [see (11)]. Because of these source terms in the circuit implementation of the ODEs, one needs to have a node corresponding to the jth region at which the sources are added. For this reason, the thermal resistance in (26) is approximated by two resistors in series, allowing for a node between them, i.e.,

$$Q_{\mathrm{cond}j} = \frac{T_{\mathrm{mid}j} - T_{\mathrm{mid}(j-1)}}{R_{\mathrm{out}j} + R_{\mathrm{in}j}}, \qquad 2 \le j \le n \tag{28}$$

where

$$R_{\mathrm{out}j} = \frac{\ln\left(r_j/r_{\mathrm{mid}(j-1)}\right)}{2\pi\kappa\left(\left[T_{\mathrm{mid}j} + T_{\mathrm{mid}(j-1)}\right]/2\right)} \tag{29}$$

$$R_{\mathrm{in}j} = \frac{\ln(r_{\mathrm{mid}j}/r_j)}{2\pi\kappa\left(\left[T_{\mathrm{mid}j} + T_{\mathrm{mid}(j-1)}\right]/2\right)}. \tag{30}$$

The approximation [see (28)–(30)] is $\mathcal{O}(\Delta^2)$ close to (19), as desired.

Using this approximation in (15) and (16) results in n ODEs, one for each region. Thus

$$\frac{dT_{\mathrm{mid}1}}{dt} = \frac{Q_{\mathrm{cond}2} + Q_{\mathrm{joule}1} - Q_{\mathrm{rad}1}}{C_{\mathrm{therm}1}} \tag{31}$$

$$\frac{dT_{\mathrm{mid}j}}{dt} = \frac{Q_{\mathrm{cond}(j+1)} - Q_{\mathrm{cond}j} + Q_{\mathrm{joule}j} - Q_{\mathrm{rad}j}}{C_{\mathrm{therm}j}}$$
$$2 \le j \le n-1 \tag{32}$$

$$\frac{dT_{\mathrm{mid}n}}{dt} = \frac{Q_{\mathrm{cond}(n+1)} - Q_{\mathrm{cond}n} + Q_{\mathrm{joule}n} - Q_{\mathrm{rad}n}}{C_{\mathrm{therm}n}}. \tag{33}$$

Equations (34)–(37) define the remaining terms used in the ODEs [see (31)–(33)], i.e.,

$$C_{\mathrm{therm}j} = A_j C_p(T_{\mathrm{mid}j})\rho(T_{\mathrm{mid}j}) \tag{34}$$

$$Q_{\mathrm{cond}(n+1)} = \frac{T_{\mathrm{water}} - T_{\mathrm{mid}n}}{R_{\mathrm{out}(n+1)}} \tag{35}$$

$$Q_{\mathrm{joule}j} = A_j E(t)^2 \sigma(T_{\mathrm{mid}j}) \tag{36}$$

$$Q_{\mathrm{rad}j} = A_j 4\pi\epsilon_0(T_{\mathrm{mid}j}). \tag{37}$$

The outermost shell has a slightly different ODE (33) than the other regions, due to the boundary condition at $r_{n+1} = R$: the temperature at the water wall is held fixed at T_{water}.

It remains to model (12) for the electric field. This is done with $i_{\mathrm{in}}(t) = E(t)G_{\mathrm{arc}}(t)$, where

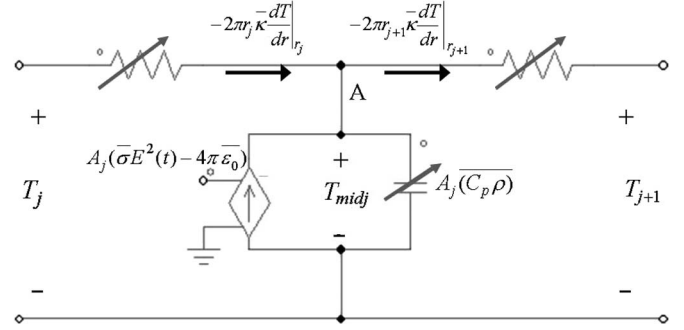$$G_{\mathrm{arc}}(t) = \sum_{j=1}^{n} A_j \sigma\left(T_{\mathrm{mid}j}(t)\right). \tag{38}$$

Fig. 3.   Thermal circuit representation of one ring-shaped arc region.

Using (38) along with (31)–(33) would result in a differential algebraic system with n ODEs and one algebraic equation. Differential algebraic systems cannot be solved via standard approaches such as MATLAB's Simulink, and for this reason, it is advantageous to include a parasitic electrical capacitance C_{in} in parallel with the electrical circuit, i.e.,

$$\frac{dE}{dt} = \frac{i_{\mathrm{in}} - EG_{\mathrm{arc}}}{C_{\mathrm{in}}}. \tag{39}$$

This parasitic capacitance would exist between the electrodes in a real lamp, although it would be so small that it would have a negligible effect on the circuit behavior. Including a parasitic capacitance creates a system of $n+1$ differential equations [see (31)–(33) and (39)] for which a wider variety of numerical solvers can be used. This is consistent with the goal of defining a model that can be used in a practical circuit design. It would be advantageous to increase the value of this capacitance to increase the convergence speed of the ODE solver so long as it does not affect the dynamics of the arc. The accuracy of the dynamics can be easily tested by observing if the dynamics change as the capacitance is increased. The capacitance has been correctly selected if changing its value has minimal impact on the dynamics.

The outputs of the model are the total arc conductance (38) and the total radiation up to time t, i.e.,

$$Q_{\mathrm{rad\_arc}}(t) = \int_0^t \sum_{j=1}^n Q_{\mathrm{rad}j}(s)ds. \tag{40}$$

IV. CIRCUIT IMPLEMENTATION

It would be useful to be able to import the arc model into a circuit simulator in order to more easily design and test a power source for the arc. A Simulink circuit implementation of the ODE model [see (31)–(33) and (39)] is therefore designed and simulated. This requires constructing the needed temperature-dependent resistors and capacitors.

A. Thermal Circuit Model

Equation (15) can be used to define a circuit where the equation describes the current entering node A in Fig. 3. The thermal circuit for each region can be connected in series to give a thermal circuit representation of the entire lamp.
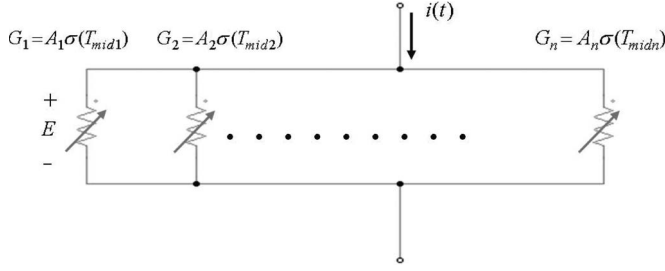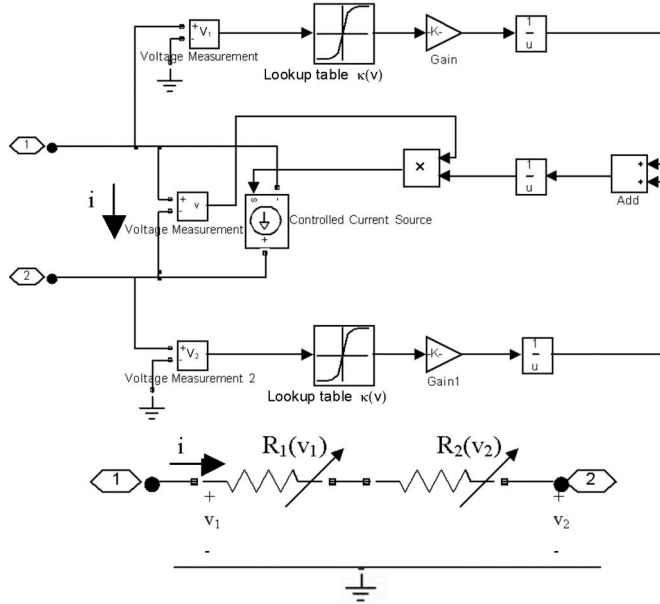
Fig. 4.   Electrical circuit for an n-region arc model.

Fig. 5.   (Top) Simulink implementation of two voltage-dependent resistors in series. (Bottom) Equivalent circuit.

It remains to present a circuit for the electric field given by (12). The conductances

$$G_j = A_j \overline{\sigma(T)}_j \qquad (41)$$

for each region are connected in parallel to form a circuit describing the per-unit length electrical behavior of the lamp. The average is taken over each shell (see Fig. 4).

The electrical and thermal circuits are linked through the temperature and electric field. The thermal resistances and capacitances, the controlled current source, and the electrical conductances all depend on temperature. The controlled current source depends on temperature and on the electric field.

B. Circuit Model of Temperature-Dependent Thermal Resistors

The series thermal resistors are implemented using a dependent current source. $R_{\text{out}j}$ and $R_{\text{in}(j+1)}$ are directly connected in series and, thus, are implemented using one current source (see Fig. 4). The circuit shown in Fig. 5 implements the following equation:

$$i = v \left(\frac{1}{G_1(v_1)} + \frac{1}{G_2(v_2)} \right)^{-1}. \qquad (42)$$
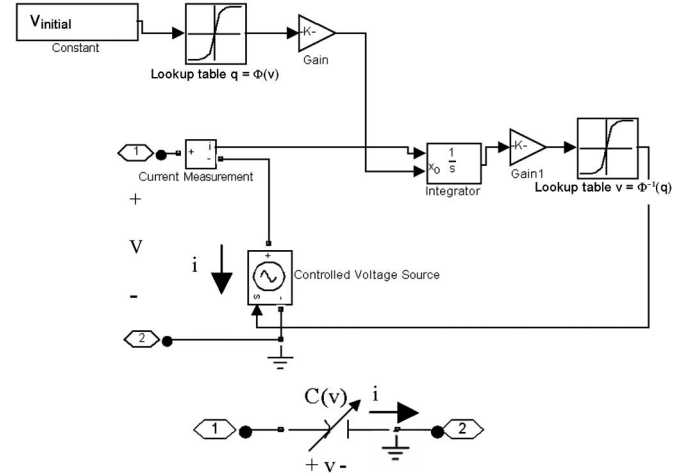

Fig. 6.   (Top) Simulink implementation of a voltage-dependent capacitor. (Bottom) Equivalent circuit.

C. Circuit Model of a Temperature-Dependent Capacitor

Implementing a nonlinear capacitor adds extra complexity as there must be a differential or integral component in the model. Integral components are advantageous as they are more stable; thus, in the case of a capacitor, the current-dependent voltage source implementation is preferred. However, this means that the capacitor must be modeled using a charge-based model. The charge Φ is a function of voltage $v(t)$, and therefore, it is a function of time, i.e., $\Phi(t) = \Phi(v(t))$. By definition, the relationship between the voltage across a capacitor and the current through it is given by

$$i(t) = \frac{d}{dt} \Phi\left(v(t)\right) = C(v)\frac{dv}{dt}. \qquad (43)$$

Integrating (43) yields

$$\Phi\left(v(t)\right) = \Phi\left(v(0)\right) + \int_0^t i(s)ds. \qquad (44)$$

If the charge is an increasing function of the voltage, then this relation can be inverted, and the voltage can be written as an increasing function of the charge. That is

$$v(t) = v\left(\Phi\left(v(0)\right) + \int_0^t i(s)ds \right). \qquad (45)$$

In the special case of a voltage-independent capacitor, $d\Phi/dv = C_0$, implying $\Phi(v) = C_0 v$ and $v(\Phi) = \Phi/C_0$.

An analogous set of equations can be developed for describing heat flow. For heat flow, the electrical charge is replaced by energy in joules, and the voltage across an electrical capacitor is replaced by a temperature difference across a thermal capacitance. The time rate of change in the charge, which is current, becomes the time rate of change in energy, which is power.

A Simulink implementation of the charge-based capacitor (45) is shown in Fig. 6. The diagram in Fig. 6 uses a current and an initial voltage difference v_{initial} as inputs. In a thermal circuit, the initial voltage is replaced by an initial temperature

T_{initial}, and the current is replaced by a power. For this model, $d\Phi/dT = C_p(T)\rho(T)$ represents the thermal capacitance as a function of the temperature difference across this capacitance. The integral with respect to T of this expression represents $\Phi(T)$, an energy, which has units of joules. The energy as a function of temperature and its inverse are found by linear interpolation from experimental data [8].

The nonlinear resistors in Figs. 3 and 4 are implemented using dependent current sources and appropriate linearly extrapolated data [8]. The Simulink representation of the sum of two thermal resistances from adjacent cells is shown in Fig. 5.

V. SIMULATIONS

The energy balance equation [see (11) and (12)] for an arc lamp is well known from the literature [9] and is taken as a benchmark. In this section, the finite-volume method (FVM) model [see (31)–(33) and (39)] is tested against the finite-element method (FEM) model of (11) and (12). The FEM model is done by COMSOL Multiphysics. This software package approximates solutions of (11) and (12) via the FEM. Rather than computing the 3-D equation [see (11)], the 1-D reduction to radial coordinates is computed. The FEM model is always computed with a large number of elements, resulting in a highly accurate numerical solution. Solutions of the FVM model [see (31)–(33) and (39)] are approximated using MATLAB's ode15s ODE solver or (when stated) in MATLAB's Simulink.

Five temperature-dependent material properties, namely, $\sigma(T)$, $\kappa(T)$, $C_p(T)$, $\rho(T)$, and $\epsilon_0(T)$, appear in the energy balance equation [see (11) and (12)]. Because the specific heat capacity $C_p(T)$ and the density $\rho(T)$ never appear separately in the equations, but only as a product (the volumetric heat capacity), $C_p(T)\rho(T)$ is treated as a single function. The gas in the arc lamp is taken to be argon at 8-bar pressure. This pressure approximately corresponds to the environment expected for the vortex water-wall arc lamp. The material properties at 8 bar are available in tabular form at 100-K intervals [8] and are implemented as functions of T via linear interpolation. Plots of $C_p(T)\rho(T)$ and $\epsilon_0(T)$ are shown in Fig. 7. $\kappa(T)$ and $\sigma(T)$ are shown in Fig. 8. In all simulations, the boundary condition at the outer wall is $T = 300$ K, and the radius of the arc is $R = 45$ mm. The parasitic capacitance in (39) is chosen to be $C_{\text{in}} = 10^{-7}$ F.

A. FEM Model

Fig. 9 shows the temperature profile for a radial cross section of the arc in response to a sinusoidal input pulse. Before the pulse, the lamp is in the steady state corresponding to a constant simmer current of 400 A. The input pulse is added to this current.

In this case, the arc retains an isothermal core, which rises and falls in temperature, but the heat capacity of the arc prevents the pulse from affecting the outer edges of the arc. As shown in Fig. 9, the core width expands at a much slower rate than the rate with which the core temperature rises and falls; in this case, the core never fully fills the lamp. The lamp cools much more
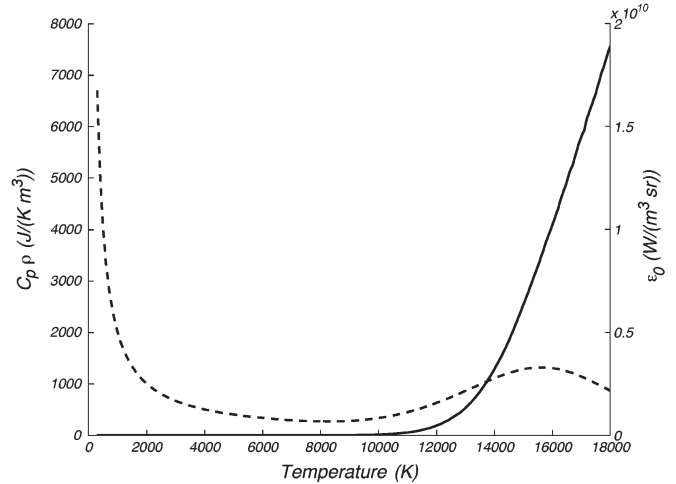

Fig. 7.   (Dashed line) Volumetric heat capacity $C_p(T)\rho(T)$ as a function of temperature for argon at 8 bar. (Solid line) Net radiative emissivity $\epsilon_0(T)$.
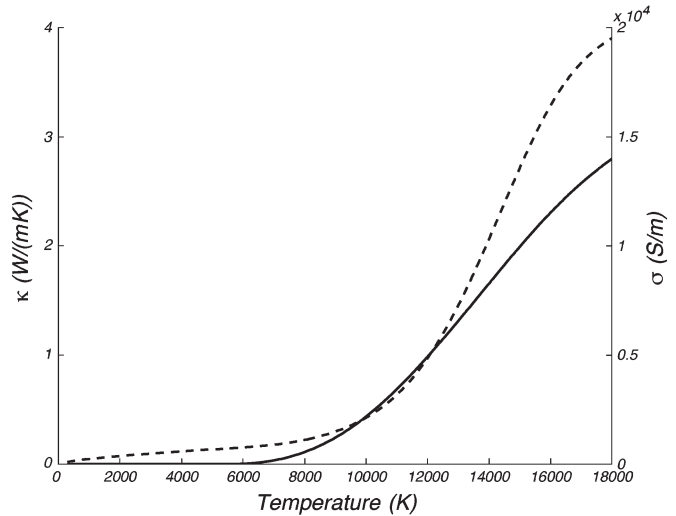

Fig. 8.   (Dashed line) Thermal conductivity $\kappa(T)$ as a function of temperature for argon at 8 bar. (Solid line) Electrical conductivity $\sigma(T)$.
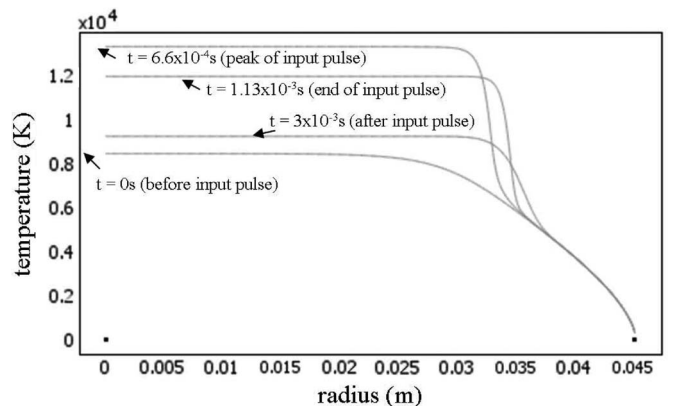

Fig. 9.   Temperature as a function of arc radius for different points in time in response to a current pulse. The input current is a sinusoidal pulse with a peak current of 40 kA, and a 1.125-ms pulsewidth is superimposed on a constant baseline current of 400 A. The temperature is approximated by (11) and (12), solved via COMSOL's FEM implementation.

slowly than it heats and continues to radiate for some time after the end of the current pulse.

B. FVM Model

First, it is checked that the spatial discretization has been correctly implemented. This is done by computing solutions of the ODEs [see (31)–(33) and (39)] with a fixed-timestep method, in this case Euler's method. A linear profile is taken for the initial temperature distribution with $T(0,0) = 320$ K and $T(R,0) = 300$ K. Approximate solutions of the ODEs [see (31)–(33) and (39)] are computed up to time $t = 0.5$. Three solutions are computed: 1) $T_{12}(r,t)$ is computed with $n = 12$ intervals of equal length and timestep $dt = 0.05$; 2) $T_{36}(r,t)$ is computed with $n = 3 \cdot 12$ and $dt = 0.05/9$; and 3) $T_{108}(r,t)$ is computed with $n = 9 \cdot 12$ and $dt = 0.05/81$. As a measure of the goodness of the method, consider the total radiation $Q_{\mathrm{rad\_arc}}(t)$ [see (40)]. For each discretization, the total radiation at time $t = 0.5$ is used in computing

$$\frac{Q_{\mathrm{rad\_arc},12}(0.5) - Q_{\mathrm{rad\_arc},36}(0.5)}{Q_{\mathrm{rad\_arc},36}(0.5) - Q_{\mathrm{rad\_arc},108}(0.5)} = 9.03. \tag{46}$$

This ratio is close to 9, confirming that the spatial discretization is at least second-order accurate, as expected. A justification for the formula used in (46) may be found in [10, p. 292].

Simulations are done to see how the arc responds to an input current of the form

$$i_{\mathrm{in}}(t) = i_0 + C\left(1 + \tanh\left(2\pi(t - 0.5)\right)\right). \tag{47}$$

This current is chosen because it starts close to i_0 at $t = 0$ and increases to the value $i_0 + 2C$ with the fastest rate of increase determined by the value of C. Taking the steady-state temperature profile corresponding to the current i_0 as initial data, the temperature profile will change in time, ultimately converging to the steady-state temperature profile corresponding to the current $i_0 + 2C$. Figs. 10 and 11 show the average temperatures and electric field for the specific case of an initial current near 400 A and a final current near 60 kA.

Fig. 10 shows results of the simulation with 12 elements, each corresponding to either a central cylinder of radius $R/12$ or a shell of width $R/12$. The average temperature of the jth region is plotted as a function of time for j between 1 and 12. The initial data correspond to a steady state for $i_0 = 400$ A; from the graph, one sees that the average temperatures for $j = 1$ to $j = 7$ are nearly the same and stay nearly the same during the evolution. This corresponds to a nearly isothermal core region from r_1 to r_8. As time passes, the core region expands and becomes hotter. The expansion is reflected in the average temperatures of the $j = 8$ to $j = 12$ shells increasing and joining the core region. The fact that the average temperature for $j = 12$ joins the core demonstrates that the simulation is not well resolved. Specifically, the boundary condition at $r_{13} = R$ is $T = 300$ K. Thus, there is a sharp transition between the core region and the boundary, all occurring within the outermost shell $r_{12} < r < r_{13}$. This shell's having an average temperature so close to the core temperature indicates that the transition layer is very thin, thinner than what is being resolved.
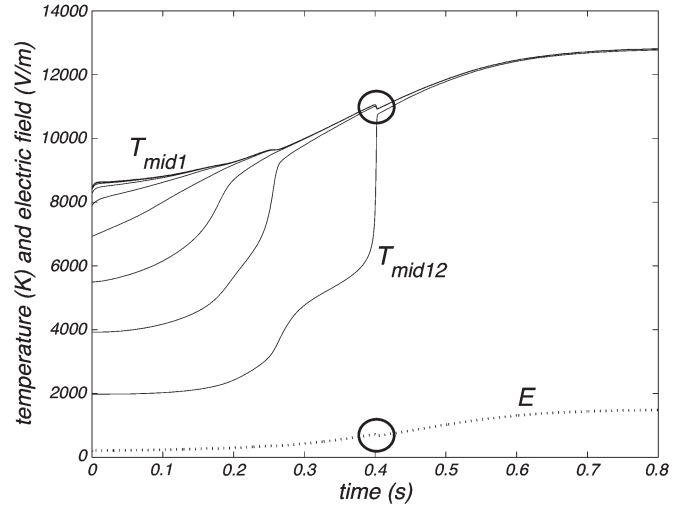

Fig. 10. Temperature for each region and arc electric field for the FVM model [see (31)–(33) and (39)] with a $\tanh$ input current (47). The arc is approximated with 12 elements, corresponding to shells of equal width. The average temperature for each shell $T_{\mathrm{mid}j}(t)$ is plotted as a function of time, along with the electric field $E(t)$. In the circled areas, one sees a sudden jump in values, which is triggered by the large abrupt change in $T_{\mathrm{mid}12}$. A sudden drop in values may be seen in the circled areas.
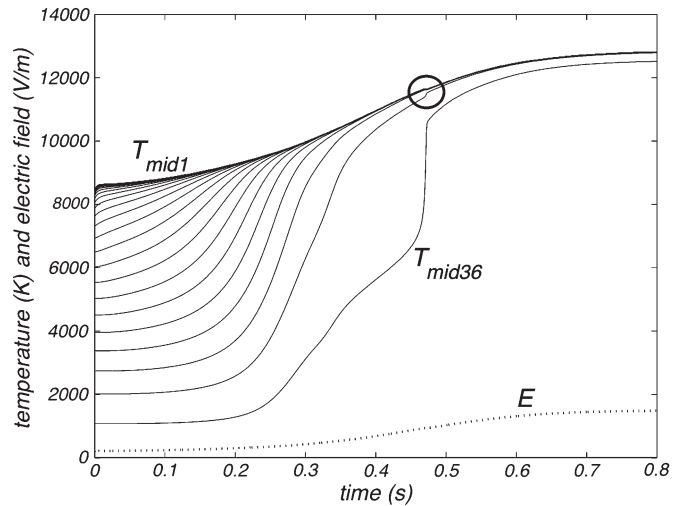

Fig. 11. Same as Fig. 10 but with 36 elements.

This underresolution is also reflected in Fig. 10 by abrupt drops in the average temperatures and electric field at certain moments in time (circled in the figure). These drops remain the same size regardless of the error tolerances set in ode15s. Thus, they appear to be an artifact of the FVM. When compared with FEM simulations using the same number of elements, the same error tolerances, and linear fitting functions for the material properties, the FVM results for the temperature at $r = r_{\mathrm{min}1}$ slightly overshoot the more accurate FEM result and then drop down slightly below the FEM result (Fig. 12).

As the number of regions is increased, the jumps in the FVM solution become smaller, and the two models become increasingly similar. Fig. 11 shows the results for the same input current but for 36 elements. Comparing this figure to the $n = 12$ figure (Fig. 10), one sees that the outermost $j = 36$ shell has its temperature increasing in time, but it does not reach
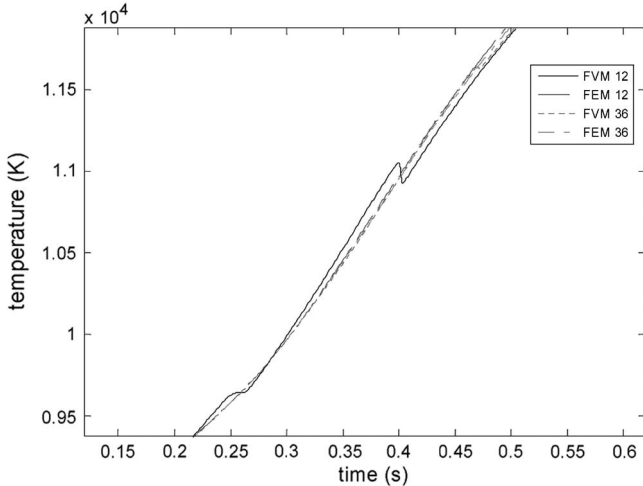
Fig. 12. Comparison of FVM and FEM temperature responses as a function of time for the innermost region (T_{mid1}).

TABLE I
TOTAL RADIATION DOSE FROM ONSET OF SIMULATION TO GIVEN TIME

radiation dose (MJ)	Matlab $n = 12$	Matlab $n = 36$	Matlab $n = 108$	COMSOL $n = 240$
at .5 ms	2.453	2.443	2.442	2.444
at .75 ms	18.31	18.20	18.35	18.32
at 1 ms	40.31	40.10	40.40	40.33

the core temperature. This is evidence that the simulation is better resolved. The average temperature for the $j = 35$ region corresponds to what was the outermost region for the $n = 12$ simulation. Both start at the value 2000 K and increase. Note that, with better resolution, one sees that this average increases more gradually. There is still a bit of an abrupt change (circled in the figure) in the simulation, occurring when the average temperature of the outermost shell makes a fast change. However, the change is smaller and slightly more gradual. There are no abrupt changes in the $n = 108$ simulation (not shown here).

It may be feasible to remove these high-frequency behaviors (abrupt changes) without significantly changing the arc behavior on the timescale of interest, for example, with the introduction of small parasitic elements linking each region in a form of feedforward filtering. This possibility should be explored.

The simulations shown in Figs. 10 and 11 are done with regions of equal width. As discussed, the core of the arc behaves in a nearly isothermal manner, and thus, there is no real need to have many regions sampling this spatial behavior. On the other hand, there is a need for sampling the behavior right outside the core and near the arc wall. For this reason, a nonuniform spatial discretization would perform better.

The radiation dose $Q_{\mathrm{rad\_arc}}(t)$ (40) is the most important final metric as it dictates the amount of heat transferred to the wafer. The radiation dose at several points in time is tabulated in Table I. The FVM model with 12 elements has relative errors that range between 0.05% and 0.4%. It is striking that a relatively underresolved simulation such as the 12-element one captures the radiation dose so well.
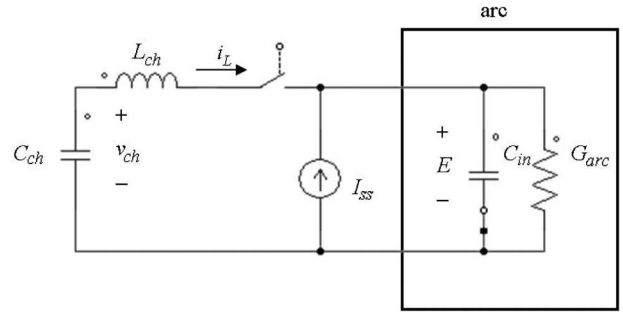

Fig. 13. Arc model including a pulse-forming circuit.

C. FVM Model With an L/C Pulse-Forming Network

The FVM model is now extended to include a simple L/C pulser circuit, as shown in Fig. 13. I_{ss} represents the simmer current, which remains between pulses and maintains the arc. The capacitor C_{ch} is initially charged with a voltage V_{ch}. The switch is closed to begin the pulse and is reopened at the next zero-crossing of the pulser current i_L. The resulting current pulse through the arc model is nearly sinusoidal in shape and is half a period in duration.

The differential equations describing the circuit are (31)–(33) and (48) for the arc itself, with i_{in} in (39) replaced by $I_{\mathrm{ss}} + i_L(t)$, giving

$$\frac{dE}{dt} = \frac{i_L + I_{\mathrm{ss}} - EG_{\mathrm{arc}}}{C_{\mathrm{in}}} \qquad (48)$$

and $i_L(t)$ is determined by (49) and (50) for the pulser, which is shown to the left of the arc in Fig. 13. The initial data are $v_{\mathrm{ch}}(0) = V_{\mathrm{ch}}$ and $i_L(0) = 0$. The function "switch(t)" is set to 1 to close the switch and reset to 0 at the next zero-crossing of the inductor current i_L to reopen the switch. This results in a single pulse. Thus,

$$\frac{dv_{\mathrm{ch}}}{dt} = -\frac{i_L}{C_{\mathrm{ch}}} \cdot \text{switch} \qquad (49)$$

$$\frac{di_L}{dt} = \frac{v_{\mathrm{ch}} - E}{L_{\mathrm{ch}}} \cdot \text{switch}. \qquad (50)$$

It remains to find reasonable values for the inductance L_{ch}, capacitance C_{ch}, and peak voltage V_{ch}. This is done by considering the L/C circuit [see (49) and (50)] in isolation. It has a pulsewidth

$$\mathrm{PW} = \pi\sqrt{L_{\mathrm{ch}}C_{\mathrm{ch}}}. \qquad (51)$$

The total energy stored in the electric field of the capacitor is transferred to the magnetic field of the inductor, which provides the pulse current for the arc. For an initial approximation, the loss caused by the arc resistance may be ignored. In isolation from (31)–(33) and (48), the pulser voltage and current, i.e., $v_{\mathrm{ch}}(t)$ and $i_L(t)$, respectively, are sinusoidal with peak amplitude V_{ch}, peak current I_L, and total energy. Thus,

$$E_J = \frac{C_{\mathrm{ch}}}{2}v_{\mathrm{ch}}(t)^2 + \frac{L_{\mathrm{ch}}}{2}i_L(t)^2 = \frac{C_{\mathrm{ch}}}{2}V_{\mathrm{ch}}^2 = \frac{L_{\mathrm{ch}}}{2}I_L^2. \qquad (52)$$
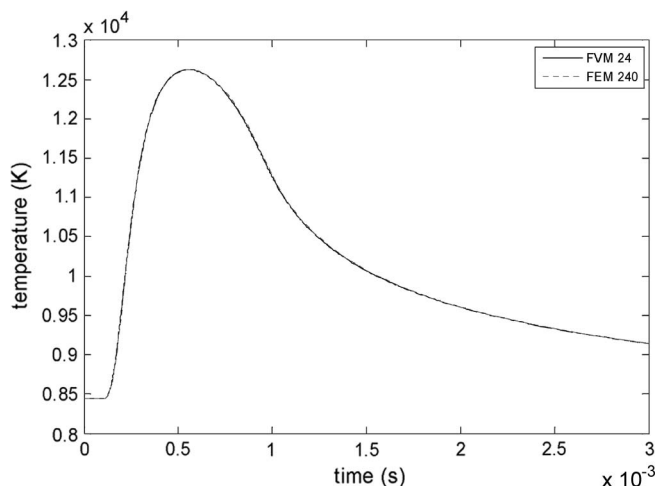
Fig. 14. The FVM model with an L/C pulse-forming network [see (31)–(33), (48), (49) and (50)] with 24 elements is considered with a 56.25-kJ pulse of width 889 μs and maximum current 26.52 kA. The central temperature $T_{\mathrm{mid1}}(t)$ is plotted as a function of time. The FEM model with 240 elements and a corresponding sinusoidal input current is also considered; the resulting central temperature is also plotted as a function of time.
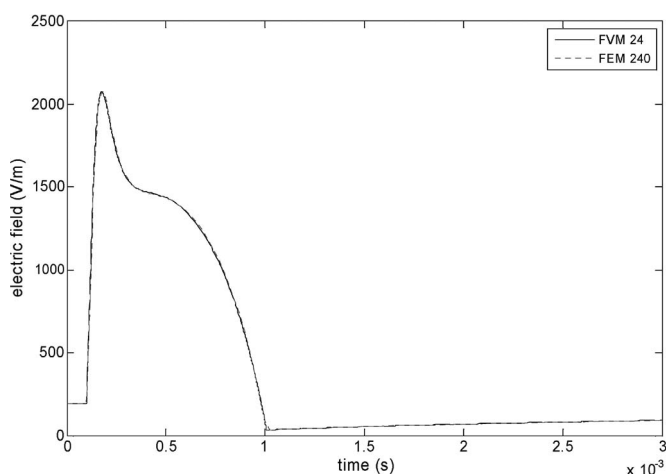

Fig. 15. The arc electric field $E(t)$ for the same simulations as discussed in Fig. 14 is plotted as a function of time.

Given the desired pulsewidth PW, peak current I_L, and total energy E_J, one chooses L_{ch}, C_{ch}, and V_{ch} to satisfy (51) and (52).

Simulations of the FVM model [see (31)–(33), (48), (49) and (50)] with a 56.25-kJ pulse of width 889 μs and peak current 26.52 kA are now considered. This can be achieved with $L_{\mathrm{ch}} = 160$ μH, $C_{\mathrm{ch}} = 500$ μF, and charging voltage $V_{\mathrm{ch}} = 15$ kV. These FVM simulations are compared with a well-resolved solution of the FEM model. Since a charging circuit cannot be easily added to the FEM model, the FEM model is run using a sinusoidal input current with amplitude and period chosen to match the current observed in the FVM model with the pulser.

The average temperature at the center of the arc, i.e., T_{mid1}, is plotted in Fig. 14, and the electric field is plotted in Fig. 15. Two versions of the FVM model are simulated in MATLAB: one version uses the ODE timestepper ode15s, and the second version uses the Simulink circuit implementation. Fig. 16 com-
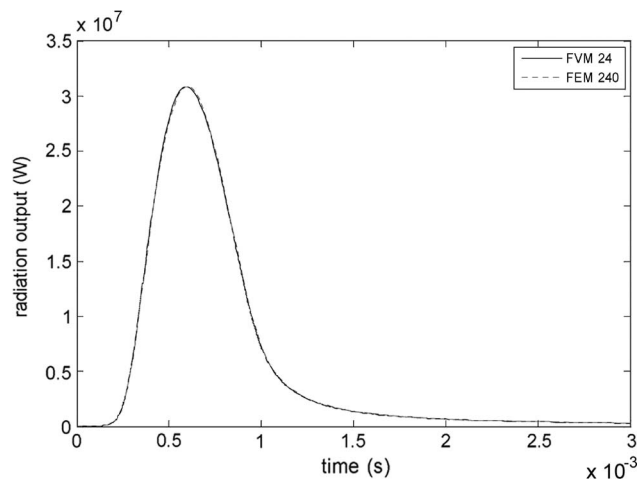

Fig. 16. The radiation dose $Q_{\mathrm{rad}_{\mathrm{arc}}}(t)$ in response to a 56.25-kJ pulse of width 889 μs is plotted as a function of time for three simulations: the 12-element FVM model with an L/C pulse-forming network with solutions computed via ode15s and via Simulink and the FEM model with 240 elements and corresponding sinusoidal input current. The 12-element FVM model has slightly higher peak radiation.

pares the arc radiation output for the two FVM implementations and the FEM model.

VI. Conclusion

A dynamic arc model is derived using averaging of the energy balance equation over spatial domains (the FVM). The space averaging approach accurately models the PDE form of the energy balance equation, as tested with both steady-state and transient arc currents, including high-energy pulses with a current amplitude range from 400 A to 27 kA and a pulsewidth of a millisecond or less.

The spatially averaged FVM model uses physical and geometric data to set the coefficients in the equations, thus avoiding the problem of system identification. In addition, the FVM model can be expressed in circuit form while giving the expected temporal v versus i and optical output characteristics.

All the simulations were done with regions of equal width. Choosing regions of different widths could result in greater accuracy with the same number of regions (or comparable accuracy with fewer regions). Thicker regions could be used near the center of the lamp, where there is a nearly isothermal core, and thinner regions could be used outside this core and close to the water wall, where the temperature strongly depends on the radius.

References

[1] T. Thrum, D. Camm, S. Dets, A. Hewett, I. Rudic, G. Stuart, and A. Viel, "Development of a powerful vortex stabilized waterwall flash lamp for RTP applications," in *Conf. Rec. IEEE IAS Annu. Meeting*, Seattle, WA, Oct. 2004, vol. 2, no. 3–7, pp. 1019–1023.
[2] J. P. Markiewicz and J. L. Emmett, "Design of flashlamp driving circuits," *IEEE J. Quantum Electron.*, vol. 2, no. 11, pp. 707–711, Nov. 1966.
[3] *High Performance Flash and Arc Lamps*, PerkinElmer Optoelectronics, Waltham, MA. (technical data sheet). [Online]. Available: http://www.perkinelmer.com/opto
[4] R. D. Garzon, *High Voltage Circuit Breakers: Design and Applications*, 2nd ed. New York: Marcel Dekker, 2002.

[5] A. M. Cassie, "Theorie nouvelle des arcs de rupture et de la rigidité des circuits," CIGRE, Paris, France, Tech. Rep. 102, 1939.
[6] O. Mayr, "Beiträge zur Theorie des statischen und des dynamischen Lichtbogens," *Arch. Elektrotech.*, vol. 37, no. 12, pp. 588–608, 1943.
[7] N. Gustavsson, "Evaluation and simulation of black-box arc models for high voltage circuit-breakers," M.S. thesis, Linköping Univ., Linköping, Sweden, 2004.
[8] *Material Property Database*, Jahm Software, North Reading, MA. [Online]. Available: http://www.jahm.com
[9] J. J. Lowke, "Characteristics of Radiation-Dominated Electric Arcs," *J. Appl. Phys.*, vol. 41, no. 6, pp. 2588–2600, 1970.
[10] K. E. Atkinson, *An Introduction to Numerical Analysis*, 2nd ed. New York: Wiley, 1989.

Francis P. Dawson (S'86–M'87–SM'07–F'09) received the B.Sc. degree in physics and the B.A.Sc., M.A.Sc., and Ph.D. degrees in electrical engineering from the University of Toronto, Toronto, ON, Canada, in 1978, 1982, 1985, and 1988, respectively.

He was a Process Control Engineer in the pulp and paper, rubber, and textile industries during the period 1978–1980. From 1982 to 1984, he was a Consultant on various projects. His development areas included high-frequency link power supplies, power supplies for specialized applications, and high-current protection circuits. Since 1988, he has been with the Department of Electrical and Computer Engineering, University of Toronto, where he is engaged in teaching and research. He has also participated as a Consultant or Project Leader in several industrial projects. His areas of research interest include static power converters and their applications, signal processing in power engineering applications, energy storage systems, and device or process modeling.

Dr. Dawson is a member of the Association of Professional Engineers of Ontario.

Basia Halliop received the B.Eng. (Hons.) degree in electrical engineering from McGill University, Montreal, QC, Canada, with a thesis exploring the modeling and simulation of thin-film photovoltaic cells, and the M.A.Sc. degree from the University of Toronto, Toronto, ON, Canada, where she worked to develop a finite-volume model of a high-temperature arc lamp for use in rapid thermal annealing. She is currently working toward the Ph.D. degree at the University of Toronto, studying interface behavior in amorphous silicon/crystalline silicon heterojunction photovoltaic cells.

Mary C. Pugh was born in Washington, DC, in 1966. She received the B.A. degree in pure mathematics from the University of California, Berkeley, in 1986, and the M.S. and Ph.D. degrees in mathematics from the University of Chicago, Chicago, IL, in 1988 and 1993, respectively.

During 1993–1997, she was a Postdoctoral Fellow with the Courant Institute, New York University, New York, and the Institute for Advanced Study, Princeton, NJ. During 1997–2001, she was an Assistant Professor at the University of Pennsylvania, Philadelphia. Since 2001, she has been an Associate Professor in the Department of Mathematics, University of Toronto, Toronto, ON, Canada. Her research is largely on the modeling, analysis, and simulation of thin films of viscous liquids, with a broader interest in computational methods for partial differential equations.